Microstructure analysis and low-cycle fatigue behavior of spray-formed Al–Li alloy 2195 extruded plate

Qingyou Zhang, Cunsheng Zhang, Jun Lin, Guoqun Zhao, Liang Chen, Hao Zhang

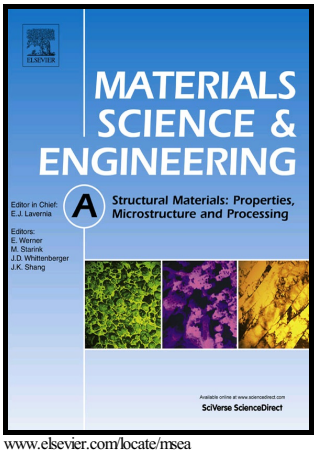

www.elsevier.com/locate/msea

PII: S0921-5093(18)31570-3
DOI: https://doi.org/10.1016/j.msea.2018.11.053
Reference: MSA37173

To appear in: *Materials Science & Engineering A*

Received date: 29 August 2018
Revised date: 10 November 2018
Accepted date: 10 November 2018

Cite this article as: Qingyou Zhang, Cunsheng Zhang, Jun Lin, Guoqun Zhao, Liang Chen and Hao Zhang, Microstructure analysis and low-cycle fatigue behavior of spray-formed Al–Li alloy 2195 extruded plate, *Materials Science & Engineering A,* https://doi.org/10.1016/j.msea.2018.11.053

Microstructure analysis and low-cycle fatigue behavior of spray-formed Al–Li alloy 2195 extruded plate

Qingyou Zhang[a1], Cunsheng Zhang[a1*], Jun Lin[a1], Guoqun Zhao[a1], Liang Chen[a1], Hao Zhang[b1]

[a]Key Laboratory for Liquid-Solid Structural Evolution & Processing of Materials (Ministry of Education), Shandong University, Jinan, Shandong 250061, P.R. China

[b]Jiangsu Haoran Spray Forming Alloy Co.,Ltd., Zhenjiang, Jiangsu 212009, P.R. China

zhangcs@sdu.edu.cn

Abstract

Microstructure and low-cycle fatigue behavior of spray-formed Al–Li alloy 2195 extruded plate were investigated in this work. The spray-formed alloy after hot extrusion experiment was treated with solid solution treatment and artificial aging. Microstructure analysis indicated the aged plate was dominated by elongated unrecrystallized grains, and had a rolling-type texture along extrusion direction with the highest intensity at Brass component. The existence of T_1 phase strengthened the alloy crucially, but δ′ phase was basically absent. Then, the fully-reversed strain-controlled low-cycle fatigue tests were conducted at total strain amplitudes ranging from 0.4% to 1.0% for samples along two orthogonal directions. The stress-strain hysteresis loops were acquired, and the cyclic stress response curves were derived. At low strain amplitudes (0.4–0.5%), the initial cyclic hardening was slight and followed by a cyclic stability, while at higher strain amplitudes (0.6–1.0%), the alloy merely presented a continuously increasing cycle hardening behavior. Moreover, the fatigue life model based on the total strain energy was built and found to be suitable to predict life. Finally, the fatigue fractography observation showed that the fatigue source is relatively concentrated and the fracture surface had typical fatigue striations at 0.5% strain amplitude, while multiple cracks originated on the sample surface and the final fracture zone showed a ductile characteristic at 1.0%. The deformed microstructure near fracture surfaces were observed, and it was found that the cyclic hardening and stability were closely associated with the interaction between moving dislocations and obstacles including (sub)grain boundaries and secondary phase particles against them.

Keywords: Spray-formed Al–Li alloy; Low-cycle fatigue; Fatigue life; Fracture morphology; Deformation

[1] Tel.: +86(0)53188392811 ; fax : +86(0)53188392811

microstructure

1. Introduction

Aluminum–lithium (Al–Li) alloys are widely used to replace conventionally 2xxx and 7xxx series aluminium alloys in the aviation and aerospace fields, due to the characteristics of low density, high elastic modulus and high mechanical strength, etc. [1, 2]. Since the first generation Al–Li alloys were developed, many efforts have been made to optimize alloying composition, improve casting methods, develop thermo-mechanical processing techniques and modify heat treatment rules for Al–Li alloys, and thus the third generation Al–Li alloys have been produced in recent years. Compared to the previous Al–Li alloys, the third generation Al–Li alloys have a superior combination among high strength, high ductility and low anisotropy, along with better fatigue resistance, corrosion resistance and thermal stability [3, 4].

The third generation Al–Li alloys, categorized as Al–Cu–Li–Mg series, have relatively higher Cu/Li ratio than the second generation Al–Li alloys with the main strengthening phase δ′ (Al_3Li), and the precipitation mechanism of Al–Cu–Li–Mg alloys are more complex: the major strengthening phase is T_1 (Al_2CuLi), while the minor phases are δ′ and θ″/θ′ (Al_2Cu) which forms from Guinier–Preston (GP) zone; there probably exist other precipitated phases such as β′ (Al_3Zr), S′ (Al_2CuMg) and Ω phase, depending on the specific alloying composition and processing condition [5, 6]. The T_1 equilibrium phase is an hexagonal platelet, the basal plane of which is parallel to the {111} Al matrix plane, and precipitates preferably on the (sub)grain boundaries and defects within grains. The effective inhibition from T_1 phase against the dislocation movement is the main reason resulting in the strengthening of Al–Cu–Li–Mg alloys [7–10].

The structural components of Al–Li alloys widely used for aerocrafts generally bear fluctuating load in service probably leading to fatigue failure, therefore the fatigue resistance performance of Al–Li alloys is a matter to be considered for the application of materials. The recent research on the fatigue resistance of Al–Li alloys is concentrated on the high-cycle fatigue (HCF) property and fatigue crack growth behavior [11–18]. On the contrary, there is relatively little research on stress response behavior, fatigue fracture model and cycle deformation mechanism of Al–Li alloys under the loading condition of low-cycle fatigue (LCF), and the related research is primarily confined to the second generation Al–Li alloys [19–21]. During the LCF process, the material generally produces a certain plastic deformation. The coherent ordered precipitates δ′ extensively distributed in the binary Al–Li alloy are susceptible to the dislocation shearing, and the subsequent dislocations tend to move along already existed slip plane leading to planer slip. Moreover, the grain boundary precipitate-free zones (PFZs) and coarse inclusion particles can contribute to this strain localization further, resulting in the local plastic deformation and

heterogeneous microstructure in the alloy. Such heterogeneity is associated with micro-void and micro-crack nucleation, causing the fatigue resistance degradation [11, 21, 22]. Notably, the third generation Al–Li alloys introduce hard-to-shear precipitates T_1 [23, 24], which leads to the transformation from planar slip to wave slip, and thus improves the deformation homogeneity of microstructure [20, 23, 25].

Lewandowska et al. [20] investigated the effect of the precipitate state on the LCF property of Al–Li alloys, and found that the addition of Cu introducing T_1 phase could make the plastic deformation of the alloy more homogeneous under cycle loading and improve the LCF life. Liu et al. [26] compared the LCF property of heat-treated and equal-channel angular pressed 8090 Al–Li alloys, and found the LCF life of heat-treated alloy was relevant to different crack propagation modes and deformation mechanisms under high and intermediate strain amplitude. The study of Wang et al. [27] indicated that the addition of scandium (Sc) could clearly change the microstructure of Al–Li alloys, including the precipitation of Sc-containing phases and the promoting S′ phase, leading to the decrease of planar slip tendency and increase of the LCF life. For other age-hardening Al alloys similar to Al–Li alloys, the LCF behavior of materials is closely associated with the characteristic of precipitated phases. Han et al. [28] studied the cyclic deformation behavior and corresponding dislocation structure evolution of Al–Cu alloy containing uniformly distributed shear-resistant precipitates, and proposed an expression for the cyclic slip irreversibility which explicitly depends on both precipitate state and plastic strain amplitude. Hockauf et al. [29] investigated the effect of precipitate morphology on the LCF property and fatigue crack growth behavior of ultrafine-grained AA6060. It was found that the newly formed coherent precipitates in the thermal recovery process could contribute to more obvious planar slip and stain localization resulting in the degradation of the LCF life.

Al–Li alloy 2195 (AA2195) studied in this work is one of the third generation Al–Li alloys, which has been gained successful applications in the lightweight fuel tanks on the space shuttle because of high specific strength and cryogenic performance [30, 31]. Spray forming is an advanced solidification technology. Different from the traditional casting process, spray-formed ingots have no macrosegregation of chemical composition, and the microstructure is more uniform and fine. Recent research has always been carried out on the effects of alloying element, heat treatment conditions and deformation process on the mechanical properties and microstructure evolution of AA2195 [32–39], but there is still very lack of literature about microstructure analysis and LCF behavior of spray-formed AA2195 extruded plate. Therefore, the following investigations will be carried out in this work. The grain micromorphology, secondary phase particles and crystallographic textures of the material will be characterized firstly. Then the LCF behavior of the alloy will be studied by performing the LCF tests with a strain-controlled tension-compression type, and the LCF life will be predicted. Finally the effects of sample

direction and strain level on the fatigue fracture mode will be investigated, and the deformation microstructure after fatigue testing will be analyzed as well.

2. Material and experiments

2. 1. Material

The experimental material is a spray-formed AA2195 extruded plate, and its chemical composition is listed in Table 1. Firstly, the alloy ingot used in this work was acquired by spray forming, and the schematic diagram of spray forming experimental setup is presented in Fig. 1(a). The detailed forming process is as follows: the deposition chamber is prefilled with argon; the alloy melt is atomized into fine droplets by high pressure argon; the cooling droplets are deposited into a billet on the rotating acceptance plate. The spray angle of refractory nozzle is 10–30°. The atomization temperature and pressure are 750–850 ℃ and 0.8 MPa, respectively. The rotating speed and descent speed of acceptance plate are 40–60 r/min and 2–4 mm/s, respectively. The as-deposited alloy ingot used in the hot extrusion experiment is Φ 560 mm × 800 mm. Then, The extrusion experiment was carried out on the 100 MN extrusion press with the extrusion die temperature of 450 ℃, billet temperature of 470 ℃, and ram speed of 0.1 mm/s, respectively. The plate with the size of 710 mm × 20 mm was extruded by a spread extrusion die. Finally, the Al–Li alloy need to undergo heat treatment to improve strength. For the purpose of good LCF property of the aged alloy, the ductility of alloy should not be reduced severely on the condition of ensuring relatively high strength. Therefore, based on our previous study, the following heat treatment rule was employed: the plate was treated with solid solution treatment at 505 ℃ for 2 h immediately followed by room-temperature water quenching, and finally artificial aging at 170 ℃ for 6 h followed by air cooling. The solution and aging treatment were performed in the heating furnace filled with argon atmosphere.

Table 1. Chemical composition of the AA2195 extruded plate (wt%).

Ag	Cu	Fe	Li	Mg	Mn	Si	Ti	Zn	Zr	Al
0.33	4.00	0.08	0.97	0.49	0.002	0.03	0.005	0.008	0.125	Bal.

2. 2. Material characterization

In this work, optical microscopy (OM, Olympus GX51) was used to observe the dimension and distribution of grains and large-sized secondary phase particles for the aged alloy. The surface preparations of metallographic samples was conducted by SiC papers and diamond slurry, then the polished surfaces were etched by Keller′s reagent (95 mL water, 2.5 mL HNO3, 1.5 mL HCI and 1.0 mL HF) through dipping the samples for 10–30 s.

Field emission scanning electron microscopy (FE-SEM, JSM-7610F) analysis was performed to observe the dimension and morphology of large-sized secondary phases and fracture surfaces of the fatigue samples in the back-scattered electron and secondary electron mode, respectively. Semi-quantitative analysis for the chemical

component of various phases was also implemented by energy-dispersive X-ray spectroscopy (EDS) equipped on the SEM.

Electron back-scattered diffraction (EBSD) measurement was carried out by SEM (FEI Nova NanoSEM 450) equipped with HKL Channel 5 analysis software to acquire grain orientation data. The mechanically polished EBSD sample needed to be electro-polished subsequently, to eliminate the effects of surface stress layer of the sample, in a mixed solution comprising 10% perchloric acid and 90% ethanol at a direct current voltage of 20 V for 10–15 s.

Transmission electron microscopy (TEM, Tecnai G2 F20 S-TWIN) with a double tilting holder was operated at an acceleration voltage of 200 kV to observe the fine precipitates and deformation microstructure, and EDS equipped on the TEM was used to identify secondary phases. The TEM samples were selected from the alloy before and after fatigue testing, and the samples after testing were taken at the distance of 2 mm from the fracture surfaces within the gauge section. The selected disc samples with a thickness of approximately 500 μm were first mechanically thinned down to below 50 μm, then the foil samples with a wedge hole could be acquired by precision ion polishing system (PIPS, Gantan691) for TEM observation.

2. 3. LCF tests

The sample preparation and experiment procedure for LCF tests were conducted according to ISO 12106: 2017 standard. The extrusion direction (ED), transverse direction (TD) and normal direction (ND) of the extruded plate were defined in this work. The fatigue samples were machined along ED and TD on the mid-plane of the plate respectively, as shown in Fig. 1(b). The geometry and size of the fatigue sample are given in Fig. 1(c). The LCF tests were performed on a Shimadu fatigue testing machine with a strain-controlled tension-compression type. A symmetrical triangular waveform was used in the tests with a strain ratio of R=-1 (i.e. a zero mean strain). The tests were conducted at room temperature with total strain amplitudes ranging from 0.4% to 1.0%, and the corresponding loading frequencies ranged from 0.5 Hz to 0.2 Hz. The strain values were recorded and controlled in time through a clip-on uniaxial extensometer with the gauge length of 12.5 mm. The tests were run under the close-loop control until final rupture of the sample.

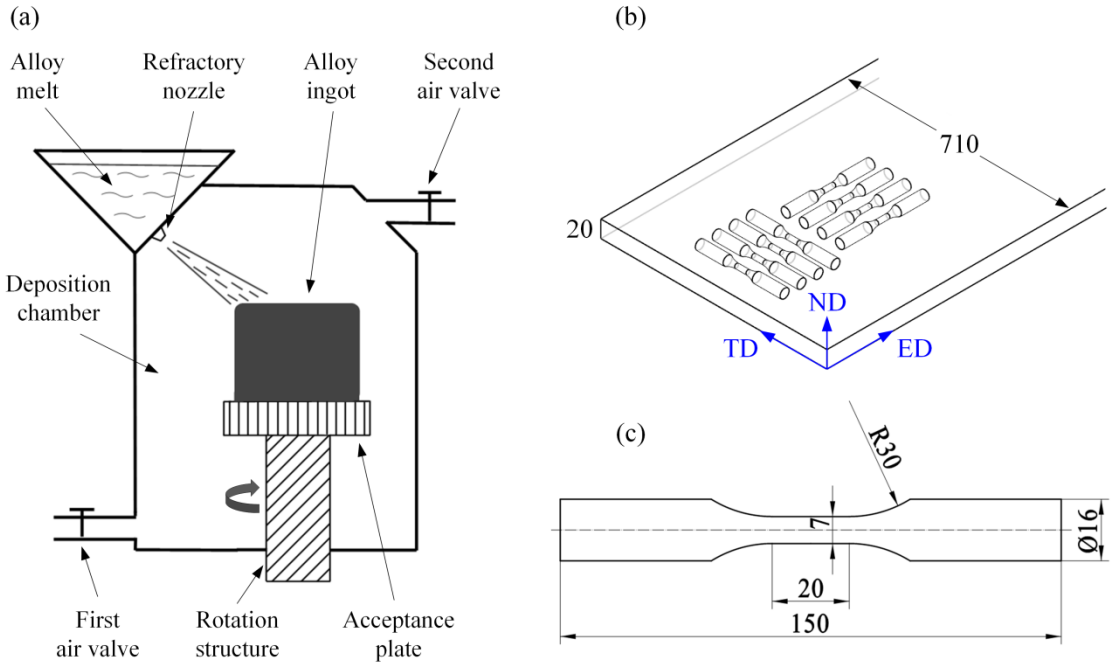

Fig. 1. (a) Schematic diagram of spray forming experimental setup; (b) schematic diagram of the LCF test sample selection from the extruded plate along ED and TD; (c) sample geometry and size (unit: mm).

3. Microstructure analysis

3. 1. Metallographic structure

The metallographic microstructure on the T–N, E–N and T–E mid-plane of the AA2195 extruded plate is given in Fig. 2. It can be seen that most grains are stretched along ED presenting a pancake-like shape with the average thickness of 16 μm, width of 80 μm and length ranging from 30 μm to 500 μm. Though the alloy underwent severe hot extrusion deformation and subsequent solution treatment, it is dominated by unrecrystallized grains. There are also some equiaxed recrystallized grains with the size of approximately 10 μm among these elongated deformed grains.

Fig. 2. Three-dimensional optical micrograph of the AA2195 extruded plate.

3. 2. Secondary phase particles

The magnified local region of metallographic microstructure on the E–N plane in Fig. 2 is given in Fig. 3(a). A number of large-sized secondary phase particles are distributed on grain boundaries and within grains. One kind of rod-like particles with the length of about 8 μm and width of about 0.8 μm on grain boundaries can be observed, and its length direction is parallel with ED. Another kind of dot-like particles with the size of below 0.6 μm is distributed both on grain boundaries and within grains, and the particles on boundaries are slightly larger than those within grains.

The microstructure on the E–N plane is magnified sequentially to further confirm the distribution and composition of large-sized secondary phases through SEM observation, as shown in Fig. 3(b), in which the similar two kinds of particles can be observed to those in Fig. 3(a). The composition identification for these particles was performed using EDS, and the results are shown in Fig. 3(c) and (d). The composition of particle 1 contains Cu and Fe except for Al element, and thus particle 1 was considered as Al_7Cu_2Fe. The EDS results are basically in agreement with the observations of Qin et al. [35] and Jiang et al. [40]. The intermetallic Al_7Cu_2Fe forms during the alloy solidification stage and remains stable, and its composition is not susceptible to the subsequent hot extrusion and heat treatment process. However, coarse Al_7Cu_2Fe particles have an adverse impact on the properties of alloy, which tends to become an initiation of fatigue crack for high-strength aluminum alloys [40]. The composition of particle 2 merely contains Cu except for Al element, so particle 2 is probably Al_2Cu, which is likely to precipitate and coarsen in the heat treatment, particularly on grain boundaries, due to high content of Cu element for AA2195 [35, 41].

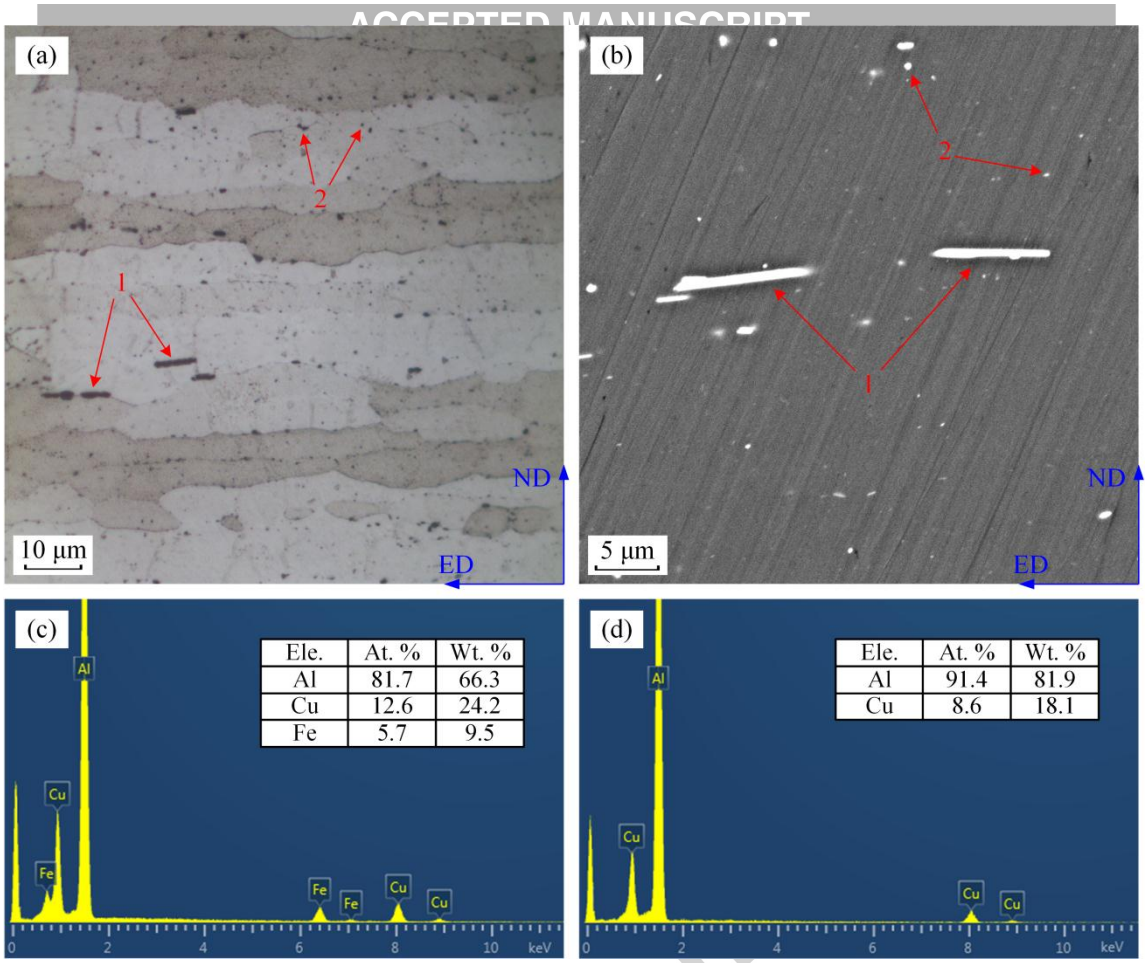

Fig. 3. (a) Optical micrograph and (b) SEM micrograph on the E–N mid-plane of the AA2195 extruded plate; EDS spot scan results of particle (c) 1 and (d) 2, respectively.

3. 3. EBSD analysis

The EBSD-derived inverse pole figure (IPF) map on the E–N plane of the extruded plate is shown in Fig. 4, in which the black and silver lines represent high-angle boundaries (grain boundary misorientation angle ≥ 15°) and low-angle boundaries (grain boundary misorientation angle between 2° and 15°), respectively. The dimension and morphology of grains with different orientations in Fig. 4 coincide with the OM microstructure on the E–N plane shown in Fig. 2. The low-angle boundaries indicate that there are some substructures within the elongated deformed grains. Moreover, for further revealing the primary crystallographic textures of the extruded plate along ED, the orientation distribution function (ODF) map was derived from EBSD, as shown in Fig. 5. The extruded plate primarily contains Brass ({110} <112>), S ({123} <634>), Cube ({100} <100>) and Copper ({112} <111>) textures according to the order from high to low intensity. The cross-section shape (i.e. aspect ratio) of extruded products affects the material flow and local stress condition during the extrusion process, and further determines the grain morphology and texture component [42–44]. For the extruded plate with high aspect ratio in this work, the alloy undergoes deformation close to plane strain during the extrusion process, leading to a pancake-like morphology and a rolling-type texture which is an incomplete β-fiber with the highest intensity at Brass

component.

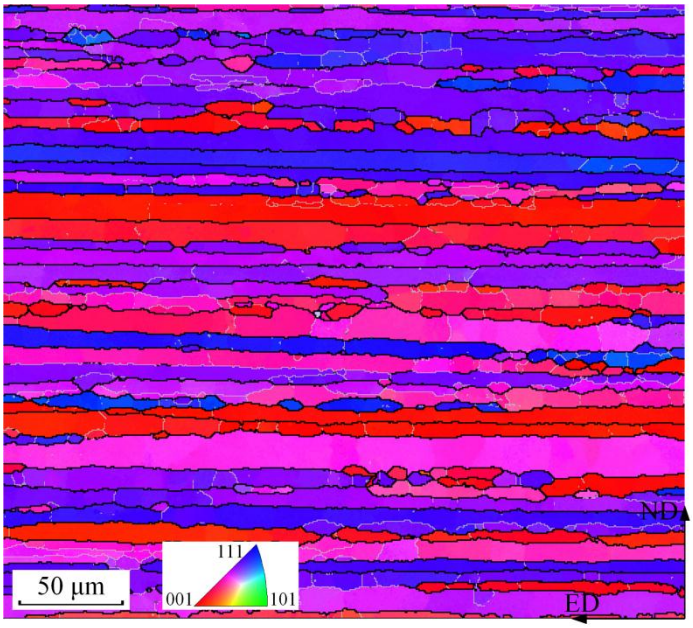

Fig. 4. EBSD-derived IPF map on the E–N mid-plane of the AA2195 extruded plate.

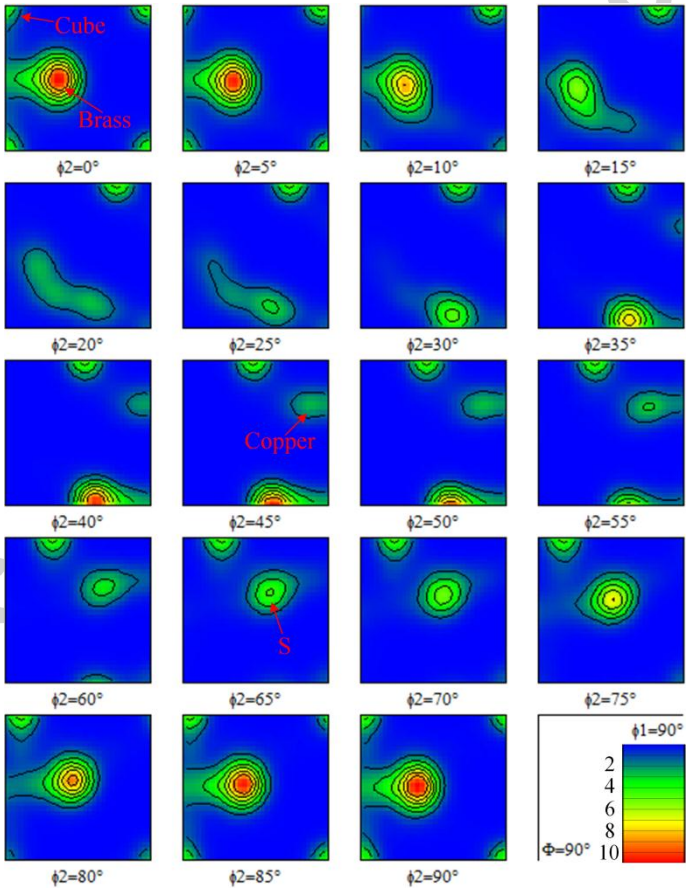

Fig. 5. EBSD-derived ODF map on the E–N mid-plane of the AA2195 extruded plate.

3. 4. TEM observation

TEM observation was carried out to analyze fine secondary phase particles of the aged AA2195. The bright-field (BF) images and selected-area electron diffraction (SAED) patterns at the corresponding region

viewed along the $<001>_{Al}$ and $<112>_{Al}$ zone axis are given in Fig. 6(a)–(d). The T_1 and θ′ phases can be observed in Fig. 6(a), and the spots at 1/3 $<220>_{Al}$ and 2/3 $<220>_{Al}$ indicate the existence of T_1 phase, while the faint streaks along $<100>_{Al}$ direction are associated with the existence of θ′ phase in Fig. 6(b) [33, 45]. The θ′ phase on the $\{100\}_{Al}$ plane is needle-like from side view, and its average length is approximately 100 nm. In addition, a small number of cubic precipitates with the size of below 25 nm can be observed in Fig. 6(a), and this phase is speculated as σ ($Al_5Cu_6Mg_2$) phase according to its feature and dimension [45–47]. From Fig. 6(c), the needle-like T1 precipitates on the $\{111\}_{Al}$ plane are distributed in the same direction and have the length of above 100 nm from side view. The spots at 1/3 $<220>_{Al}$ and 2/3 $<220>_{Al}$ and streaks along $<111>_{Al}$ direction indicate the existence of T_1 phase in Fig. 6(d) [33]. Both T_1 and θ′ phases, which exist as obstacles against the movement of dislocations, play a vital role in the strengthening of aged AA2195. It is worth noting that the superlattice spots of δ′ phase are not observed in SAED patterns, and thus the δ′ phase is considered to be basically absent in the alloy which was aged at 170 ℃ for 6 h, which may diminish the effect of dislocation shearing on the strain localization. For AA2195 with the Cu/Li ratio up to 4, it is reasonable that the δ′ phase is probably absent due to the competition of T_1 phase with δ′ phase [48].

The grain boundaries, secondary phase particles and PFZs around grain boundaries are given in Fig. 6(e). Because PFZs are generally weaker than the matrix, stress concentration tends to occur within the PFZs preferentially, and the severe plastic deformation in this position contributes to the accumulation of fatigue damage [49]. However, PFZs observed in Fig. 6(e) are not obvious, which indicates that the heat treatment condition in this work does not result in the excessive precipitation and aggregation of secondary phases on grain boundaries, thus relieving the adverse effect of PFZs on fatigue failure. The primary compositions of secondary phases were analyzed by EDS, as listed in Table 2. The coarse particle A distributed on grain boundaries has a size of above 200 nm in an irregular shape, and contains high Cu content. This particle is speculated as Al_2Cu, which coincides with particle 2 in Fig. 3. The globular particle B and C distributed on grain boundaries and within grains respectively, both have a diameter of approximately 50 nm. These particles contain high Zr content, and are speculated as β′ phase. Coherent ordered precipitates β′ can play a certain role in hindering the recrystallization of alloy [43, 50, 51]. Therefore, the extruded plate through solution treatment still remains an unrecrystallized microstructure and has strong texture components along ED.

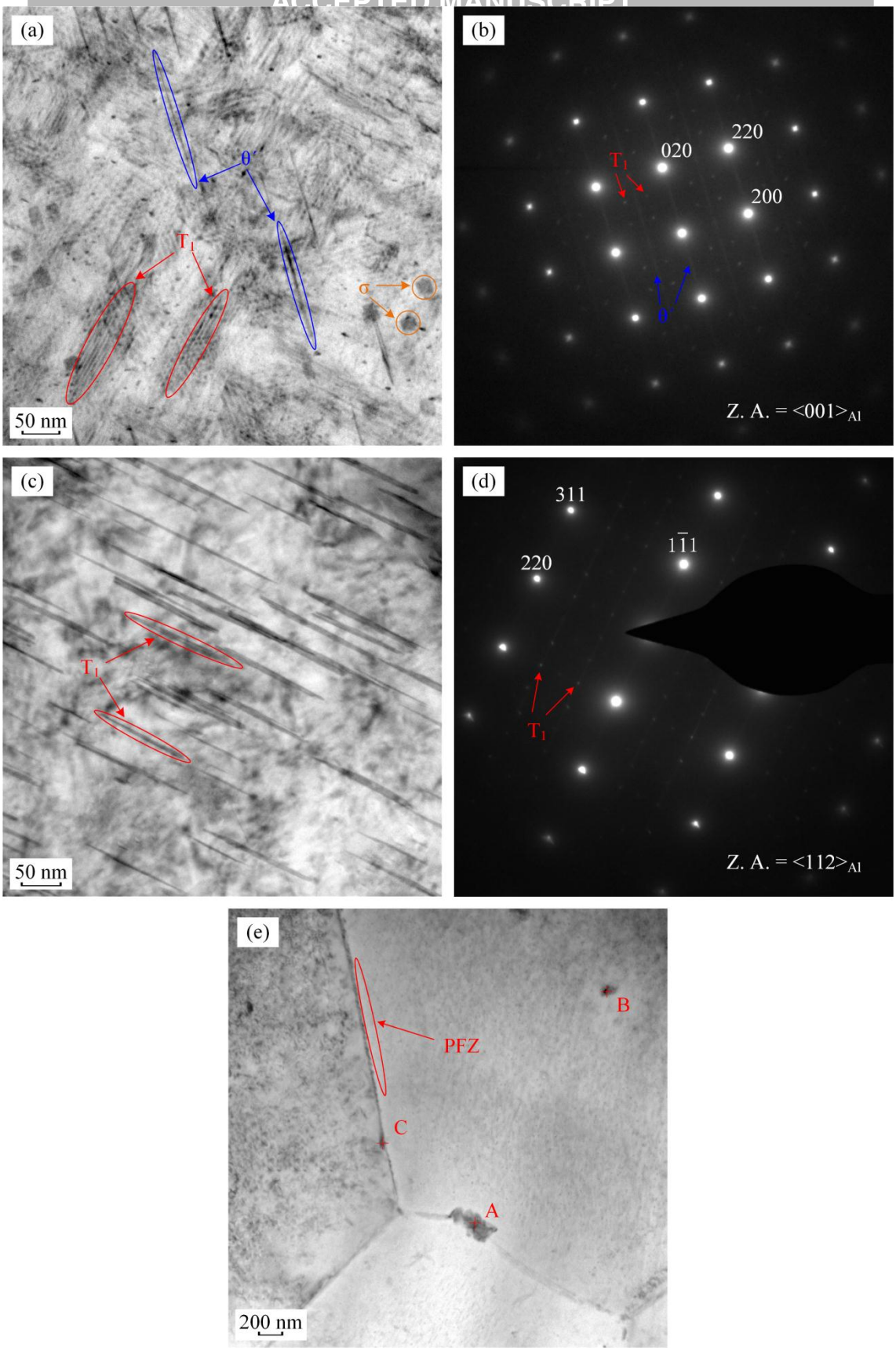

Fig. 6. TEM BF images and the corresponding SAED patterns of the aged AA2195 viewed along the (a), (b) $<001>_{Al}$ and (c), (d) $<112>_{Al}$ zone axis; (e) TEM BF image for grain boundaries of the alloy.

Table 2. Primary chemical composition of secondary phases analyzed by EDS spot scan.

Element	A		B		C	
	at.%	wt.%	at.%	wt.%	at.%	wt.%
Al	87.51	75.87	89.83	73.77	87.37	68.51
Cu	10.27	20.97	1.43	2.76	1.33	2.45
Zr	0	0	7.99	22.17	10.61	28.12
Ag	0.53	1.84	0.29	0.96	0.17	0.54
Mg	1.69	1.32	0.46	0.34	0.52	0.37

4. LCF behavior analysis

4. 1. Stress-strain hysteresis loops

The strain-controlled LCF tests for samples along TD and ED were conducted to get cycle stress-strain hysteresis loops, and their area represents the degree of cycle plastic deformation of material. The comparison between hysteresis loops at initial cycle (IC) and mid-life cycle (MC) under varying total strain amplitudes ranging from 0.4% to 1.0% for TD and ED samples is given in Fig. 7. From the figure, all hysteresis loops at any strain amplitude are almost symmetrical, which indicates that material has a similar deformation behavior in the tensile and compressive stage of cycle loading. However, the shapes of MC hysteresis loops are generally longer and narrower than those at IC, so the cycle stress amplitude is higher and the cycle plastic strain is lower at MC.

With the increase of strain amplitude, the area of hysteresis loops at both IC and MC increases, and more plastic deformation occurs for both TD and ED samples. At the strain amplitude of 0.4%, both IC and MC hysteresis loops are very narrow almost like a line, which indicates that material is basically in elastic deformation state and plastic strain is absent under cycle loading, showing a purely elastic fatigue behavior. At the strain amplitudes of 0.5% and 0.6%, the plastic strain begins to appear in IC hysteresis loops, but with the cycle loading, MC hysteresis loops become much narrower and the plastic strain has disappeared. However, with increasing strain amplitude to 0.7%, 0.8% and 1.0%, the cycle deformation is dominated by plastic strain in both IC and MC hysteresis loops.

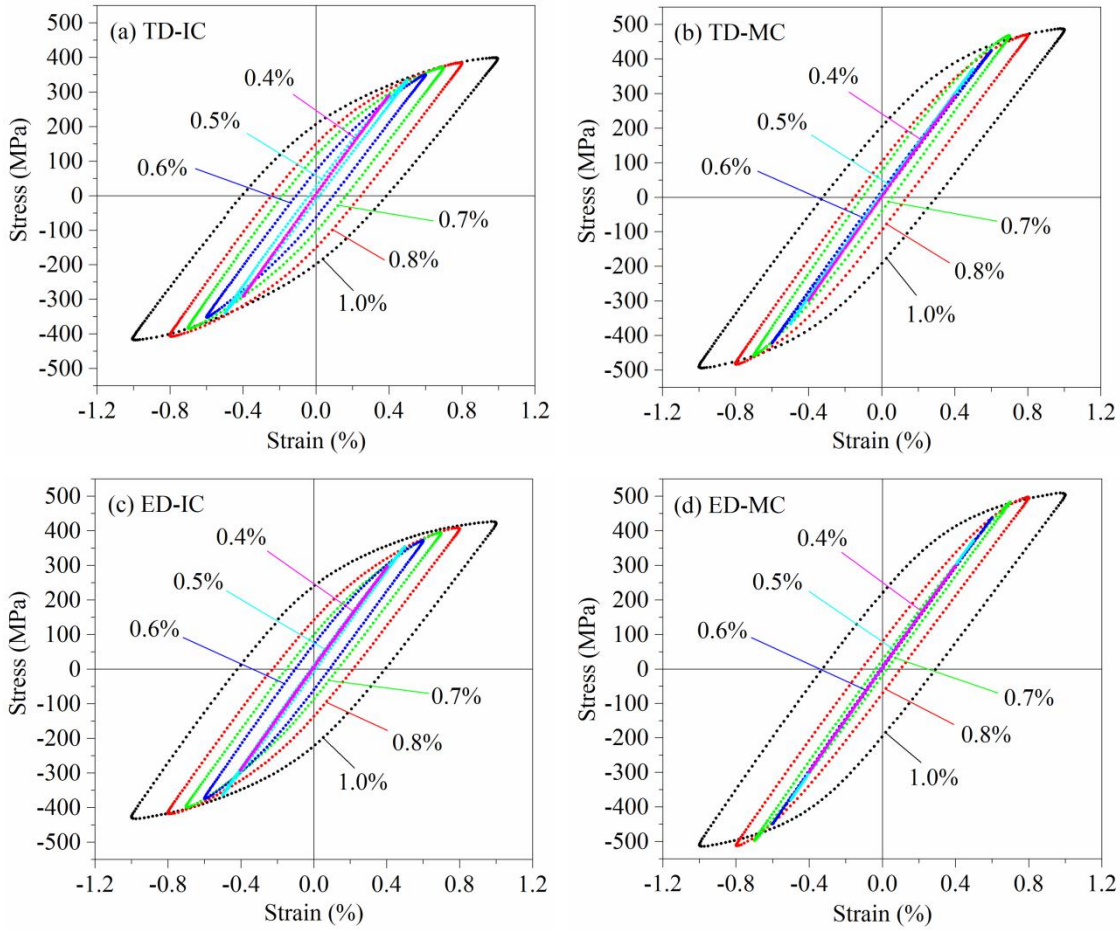

Fig. 7. IC and MC cycle stress-strain hysteresis loops under varying total strain amplitudes ranging from 0.4% to 1.0% for (a), (b) TD and (c), (d) ED samples.

The comparison of hysteresis loops of TD and ED samples at the strain amplitudes of 0.5% and 1.0% is given in Fig. 8. At the strain amplitude of 0.5%, IC hysteresis loops along ED are longer and narrower than those along TD, and the stress amplitude is higher and the plastic strain is lower along ED. This comparison also indicates that aged AA2195 extruded plate has a higher yield strength along ED. MC hysteresis loops along TD and ED are more similar, but a slightly higher stress amplitude is found along ED. However, at higher strain amplitude such as 1.0%, an obvious yield behavior is observed, and both IC and MC hysteresis loops along ED have a higher stress amplitude than those along TD.

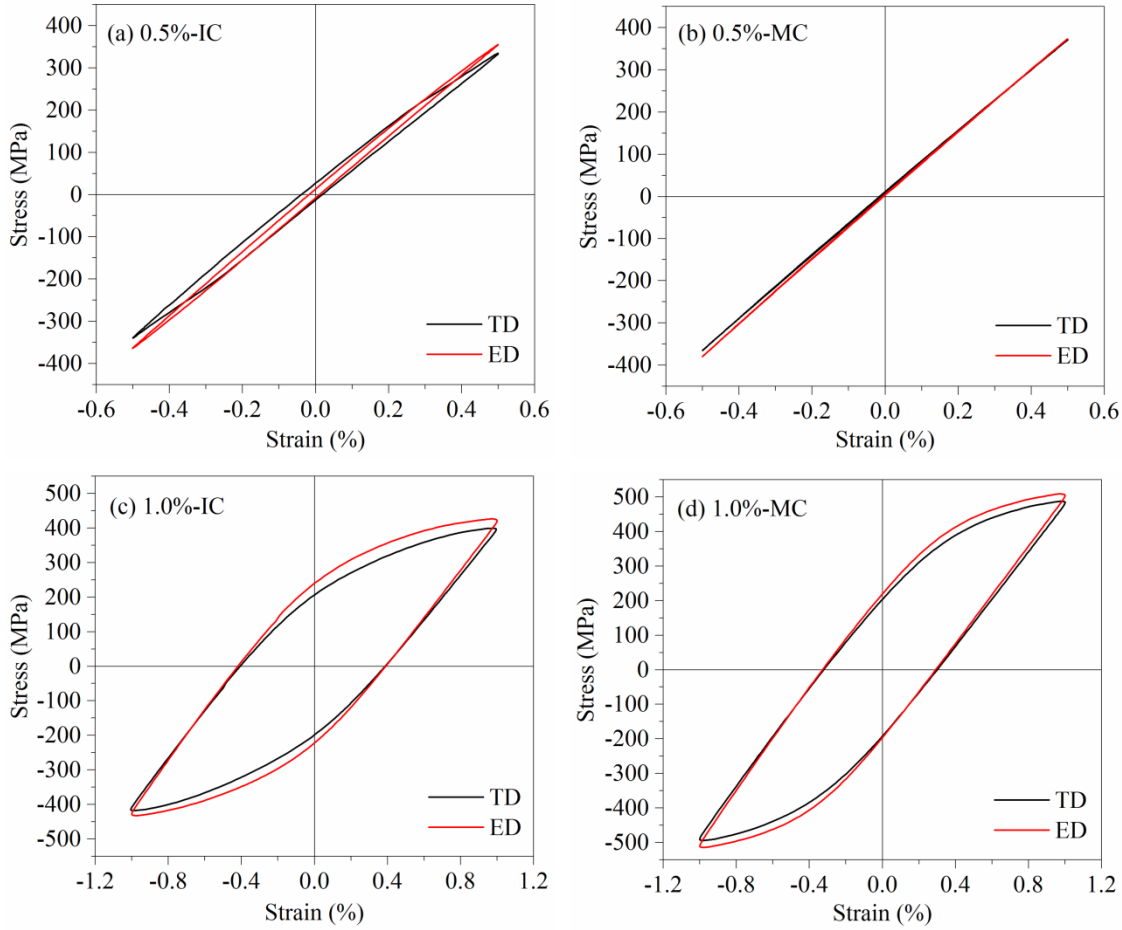

Fig. 8. Comparison of IC hysteresis loops and comparison of MC hysteresis loops for TD and ED samples at the selective strain amplitudes of (a), (b) 0.5% and (c), (d) 1.0%.

4. 2. Cyclic stress response behavior

The evolution of cyclic stress amplitude with the number of cycles at varying total strain amplitudes for TD and ED samples is shown in Fig. 9. In general, the strain amplitude has an obvious effect on the cycle characteristics of material. With the increase of strain amplitude, the corresponding stress amplitude increases and fatigue life decreases. Under each strain condition, the stress amplitude always increases with the number of cycles, showing the cycle hardening behavior, which is consistent with the variation of hysteresis loops from IC to MC. Moreover, there is no obvious difference in the fatigue life for TD and ED samples at the same strain condition, but ED samples could bear higher stress under cycle loading.

At the strain amplitude of 0.4%, the evolution of stress amplitude for TD and ED samples is similar. The cycle hardening is very slight in the early loading stage, and followed by a stress plateau after approximately 1500 cycles for both TD and ED samples, which presents a characteristic of cycle stability until fatigue fracture of material. At the strain amplitude of 0.5%, the early cycle hardening and subsequent cycle stability are also observed, and the stress plateau appears after about 3500 cycles for both samples. However, the stress amplitude for ED samples is 20 MPa higher than that for TD samples under initial loading, while the difference of stress

amplitude is reduced to merely 8 MPa gradually. At higher strain amplitudes (0.6–1.0%), the parallel stress amplitudes always increase continuously and rapidly for TD and ED samples with the increasing number of cycles, and there is no stress plateau in the whole loading stage, suggesting an obvious cycle hardening behavior. Moreover, the stress amplitude for ED samples is always about 20 MPa higher than that for TD samples.

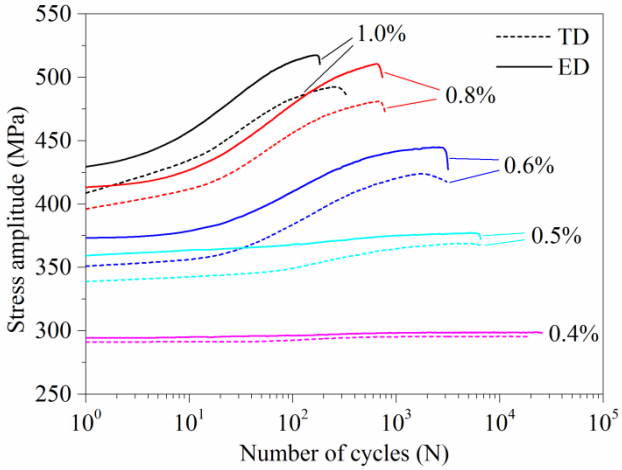

Fig. 9. Cyclic stress amplitude versus the number of cycles at varying total strain amplitudes ranging from 0.4% to 1.0% for TD and ED samples.

From above analysis, the cycle stress amplitude along ED is always higher than that along TD under each strain condition for the extruded plate, which is caused by the elongated unrecrystallized microstructure and strong texture components along ED, as described in Section 3. However, an interesting phenomenon is observed that the evolution of stress amplitude along TD is basically parallel to that along ED with the increasing number of cycles for each strain condition except for 0.5%. At the strain amplitude of 0.5%, the difference in stress amplitude between ED and TD samples reduces gradually during cycle loading, which can be explained by that an more obvious plastic deformation occurs along TD than ED as shown in Fig. 8 [52]. This phenomenon also indicates that, under the deformation condition of far away from the yield point, the grain morphology and crystallographic texture may not be the main factor influencing the stress evolution tendency.

4. 3. Fatigue life

The cycle stress-strain relation for AA2195 along TD and ED can be described by the following Hollomon equation:

$$\frac{\Delta\sigma}{2} = K'(\frac{\Delta\varepsilon_p}{2})^{n'} \quad (1)$$

where K' is the cyclic strength coefficient, n' is the cyclic strain hardening exponent, $\Delta\sigma$ is the cycle stress range and $\Delta\varepsilon_p$ is the corresponding plastic strain range. Thereinto, $\Delta\sigma$ and $\Delta\varepsilon_p$ are acquired on the basis of the stress-strain hysteresis loops at MC. Taking into account the linear relation between stress and elastic strain

(expressed by Hooke′s law), the relation of total strain amplitude versus stress amplitude is derived as follows:

$$\frac{\Delta\varepsilon_t}{2}=\frac{\Delta\varepsilon_e}{2}+\frac{\Delta\varepsilon_p}{2}=\frac{\Delta\sigma}{2E}+\left(\frac{\Delta\sigma}{2K'}\right)^{1/n'} \tag{2}$$

where $\Delta\varepsilon_t$ is the total strain range, $\Delta\varepsilon_e$ is the elastic strain range and E is Young's modulus. Therefore, the cycle stress-strain curves for TD and ED samples are plotted in Fig. 10, and the parameter values of K', n' and E are obtained by linear-regression analysis, as listed in Table 3.

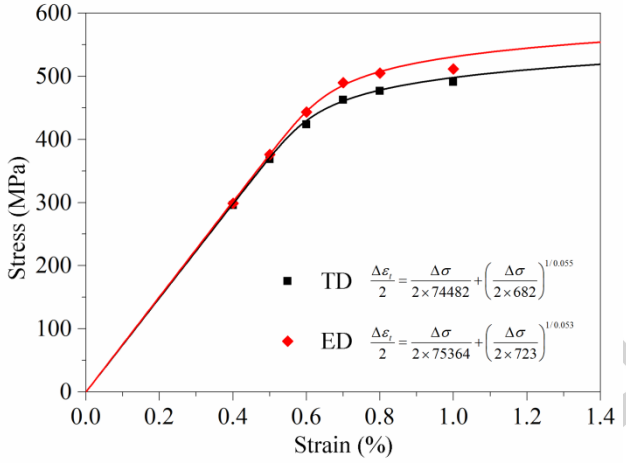

Fig. 10. Cycle stress-strain curves for TD and ED samples.

Table 3. Low cycle fatigue parameters for TD and ED samples.

Low cycle fatigue parameters	TD	ED
Cyclic strength coefficient K' (MPa)	682	723
Cyclic strain hardening exponent n'	0.055	0.053
Young's modulus E (GPa)	74.48	75.36
Fatigue damage coefficient κ'_p (GJ/m^3)	475.62	174.23
Fatigue damage exponent α'_p	-1.73	-1.64
Fatigue damage coefficient κ'_t (MJ/m^3)	383.26	168.31
Fatigue damage exponent α'_t	-0.63	-0.53

In order to predict the LCF life of material, a number of fatigue life models have been developed by introducing different fatigue damage parameters [53–55]. According to the defined parameters, these models can be classified into stress-based, strain-based and energy-based ones. The effect of strain or stress amplitude on fatigue life is generally neglected in the stress-based or strain-based models, respectively. Therefore, the strain energy of hysteresis loops is used to replace stress or strain as a fatigue damage parameter, and the interrelation between stress and strain could also be considered. In addition, The energy-based models are able to reflect the fatigue damage mechanism better [53].

The LCF life of material is largely dependent on the plastic deformation under cycle loading. Therefore, the plastic strain energy density is taken as a fatigue damage parameter, and the energy-based Halford–Marrow equation is used for life prediction [52,56,57]:

$$\Delta W_p = \kappa'_p (2N_f)^{\alpha'_p} \tag{3}$$

where ΔW_p is the plastic strain energy density per cycle and N_f is the fatigue life. In addition, κ'_p is the fatigue damage coefficient which is a material constant representing the fatigue damage capacity, while α'_p is the fatigue damage exponent indicating the ability of defusing fatigue damage. With the increase of κ'_p and decrease of $|\alpha'_p|$, more plastic strain energy can be absorbed and dissipated, thus exhibiting stronger resistance of fatigue damage. The plastic strain energy density ΔW_p can be obtained from the following calculation formula：

$$\Delta W_p = \frac{1-n'}{1+n'} \Delta\sigma\Delta\varepsilon_p \tag{4}$$

where the cyclic strain hardening exponent n' is acquired in Eq. (1). The power law relation between the plastic strain energy density ΔW_p and the number of reversals to fatigue failure $2N_f$ on the log-log scale for TD and ED samples is given in Fig. 11(a). The material constants κ'_p and α'_p are acquired through the linear-regression analysis, as listed in Table 3. The ΔW_p–$2N_f$ function relationship clearly reflects that the fatigue life decreases with the increase of plastic strain energy. The correlation between predicted fatigue life calculated based on Eq. (3) and experimental life for TD and ED samples is presented in Fig. 11(b). The diagonal solid line represents the perfect match between predicted and experimental life, while the other two dashed lines stand for the bounds of a factor of 2. All data points are located within the bounds, and the life data for TD samples are much closer to the diagonal line than those for ED ones, which means that this fatigue life model has a better prediction for AA2195 along TD.

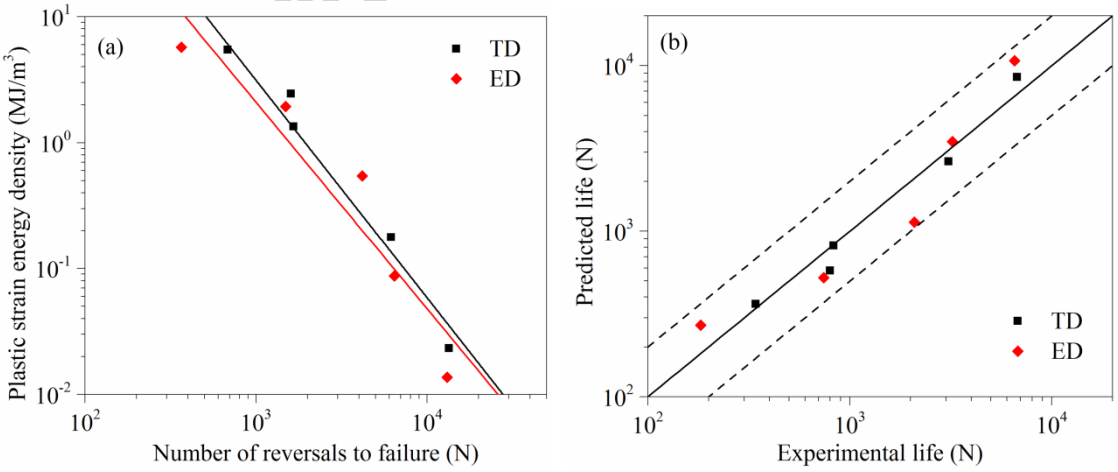

Fig. 11. (a) The number of reversals to fatigue failure versus the plastic strain energy density; (b) correlation between predicted fatigue life calculated based on Eq. (3) and experimental fatigue life for TD and ED samples.

However, at low total strain amplitude, little plastic deformation appears, and the plastic strain energy of hysteresis loops is close to zero as shown in Fig. 7. The fatigue failure possibly occurs in the HCF stage or the transition stage between LCF and HCF. Therefore, under the condition of low strain level, the application of the life prediction model merely based on the plastic strain energy density is hindered. This is the reason why the 0.4% strain amplitude in this work is not considered in the above model. Moreover, neglecting the effect of elastic strain energy on fatigue life is inappropriate in terms of fatigue damage mechanism. Therefore, the total strain energy density containing elastic and plastic portion is proposed reasonably as a fatigue damage parameter to predict fatigue life [58, 59].

The total strain energy density ΔW_t is divided into the plastic strain energy ΔW_p, and the elastic strain energy ΔW_e^+ associated with the tensile portion which facilitates crack growth. The power law relation between the plastic strain energy density ΔW_t and the number of reversals to fatigue failure $2N_f$ is established as follows:

$$\Delta W_t = \Delta W_e^+ + \Delta W_p = \kappa_t'(2N_f)^{\alpha_t'} \tag{5}$$

where κ'_t and α'_t are the fatigue damage coefficient and exponent based on the total strain energy respectively. The positive elastic strain energy ΔW_e^+ can be obtained from following calculation formula:

$$\Delta W_e^+ = \frac{\sigma_{\max}^{\ 2}}{2E} = \frac{1}{2E}\left(\frac{\Delta\sigma}{2} + \sigma_m\right)^2 \tag{6}$$

where $\sigma_{\max}$ and σ_m are the tensile peak stress and mean stress of MC hysteresis loops respectively. The ΔW_t–$2N_f$ relation on the log-log scale for TD and ED samples is given in Fig. 12(a), and the material constants κ'_t and α'_t are acquired, as listed in Table 3. The ΔW_t–$2N_f$ function relationship clearly reflects that the fatigue life decreases with the increase of total strain energy. The correlation between predicted fatigue life calculated based on Eq. (5) and experimental life for TD and ED samples is presented in Fig. 12(b). All data points are found to locate within the bounds of a factor of 1.5 which two dashed lines denote. Therefore, in contrast with the fatigue life model based on the plastic strain energy, the model based on the total strain energy could give a more accurate prediction for AA2195 in both sample directions.

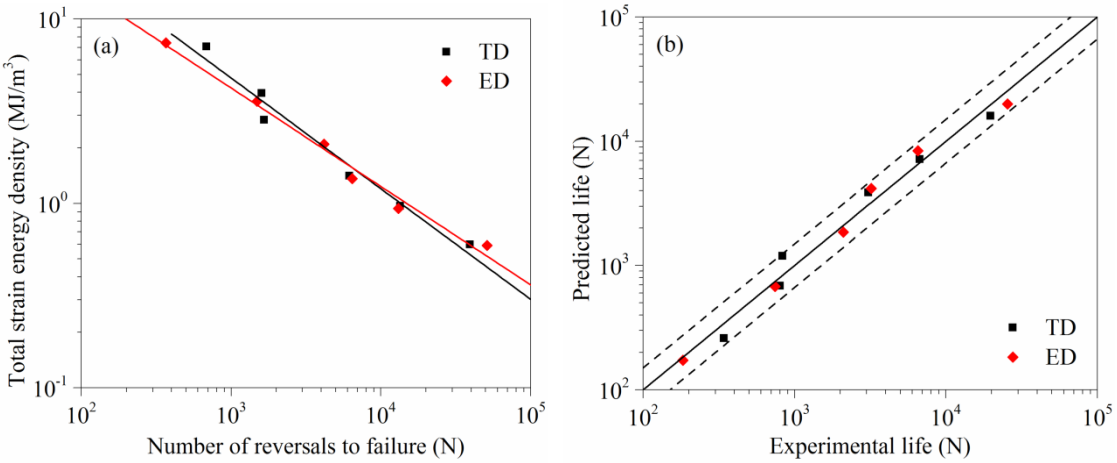

Fig. 12. (a) The number of reversals to fatigue failure versus the total strain energy density; (b) correlation between predicted fatigue life calculated based on Eq. (5) and experimental fatigue life for TD and ED samples.

5. Fatigue fractography and deformation microstructure

5. 1. Fatigue fractography at low strain amplitude

Fig. 13 gives the fatigue fractography of TD samples at the strain amplitude of 0.5%. The typical fatigue fractography is observed, which consists of fatigue crack initiation (FCI) zone (including early crack growth), fatigue crack growth (FCG) zone and final fracture zone. The low magnification morphology is shown in Fig. 13(a), and the FCI zone is marked by the red arc line. The morphology in the orange rectangle region in Fig. 13(a) is magnified as Fig. 13(b). The cracks originate at the sample surface, and propagate toward the inside of the material. The FCI zone presents a radial pattern, and the radial lines near the fatigue source don't fully converge at one point, suggesting that more than one FCI source may be concentrated in this region. From Fig. 13(b), the crack initiation is located within the coarse extrusion-intrusion region at the sample surface. Due to the irreversible dislocation movement inside the surface grains, the persistent slip bands form and increase during the cycle loading, leading to the formation of the above extrusion-intrusion region. Moreover, A few oxide inclusions are observed near the fatigue source, which promote the generation of fatigue source.

The transition zone from early crack growth to stable crack growth is shown in Fig. 13(c), and the crack propagation direction is marked by the blue arrow. In the left side of Fig. 13(c), the region with radial lines shows a crystallography characteristic that different fracture facets connect with each other leading to the formation of cleavage steps. In the right of the figure, the fatigue striations with quite small spacing are observed, indicating that the crack propagation mode gradually turns to stable growth. In addition, there are some tiny holes locally, which may be caused by the separation of second phase particles. The noteworthy FCG zone is presented in Fig. 13(d)–(g) which are in the order of crack propagation, and this zone has a typical characteristic of fatigue striations. Fatigue striations are generally caused by repeated tension-blunting and compression-sharpening of

cracks in the plastic deformation region in front of the fatigue crack tip. The fatigue striations with a shape of curved waves are basically parallel to each other, and perpendicular to the direction of local crack propagation. It is interesting that the faint grain morphology on the E–N plane of the alloy can be seen in this FCG zone. The crack propagation directions within different grains have a slight difference because of the disturbance of grain boundaries against the crack advance. From Fig. 13(d)–(g), with the crack propagation, the width of fatigue striations increases gradually. Moreover, in the late stage of stable crack growth, some secondary cracks parallel to striations (observed in Fig. 13 (f) and (g)) and a few obvious dimples around striations with relatively large spacing (observed in Fig. 13 (g)) appear. In the final fracture zone in Fig. 13(h), a number of dimples with different sizes and depths are observed presenting a ductile fracture characteristic, and there are some secondary phase particles such as Al_7Cu_2Fe in certain dimples. In addition, some partial cleavage facets and tear ridges can also be found in this region.

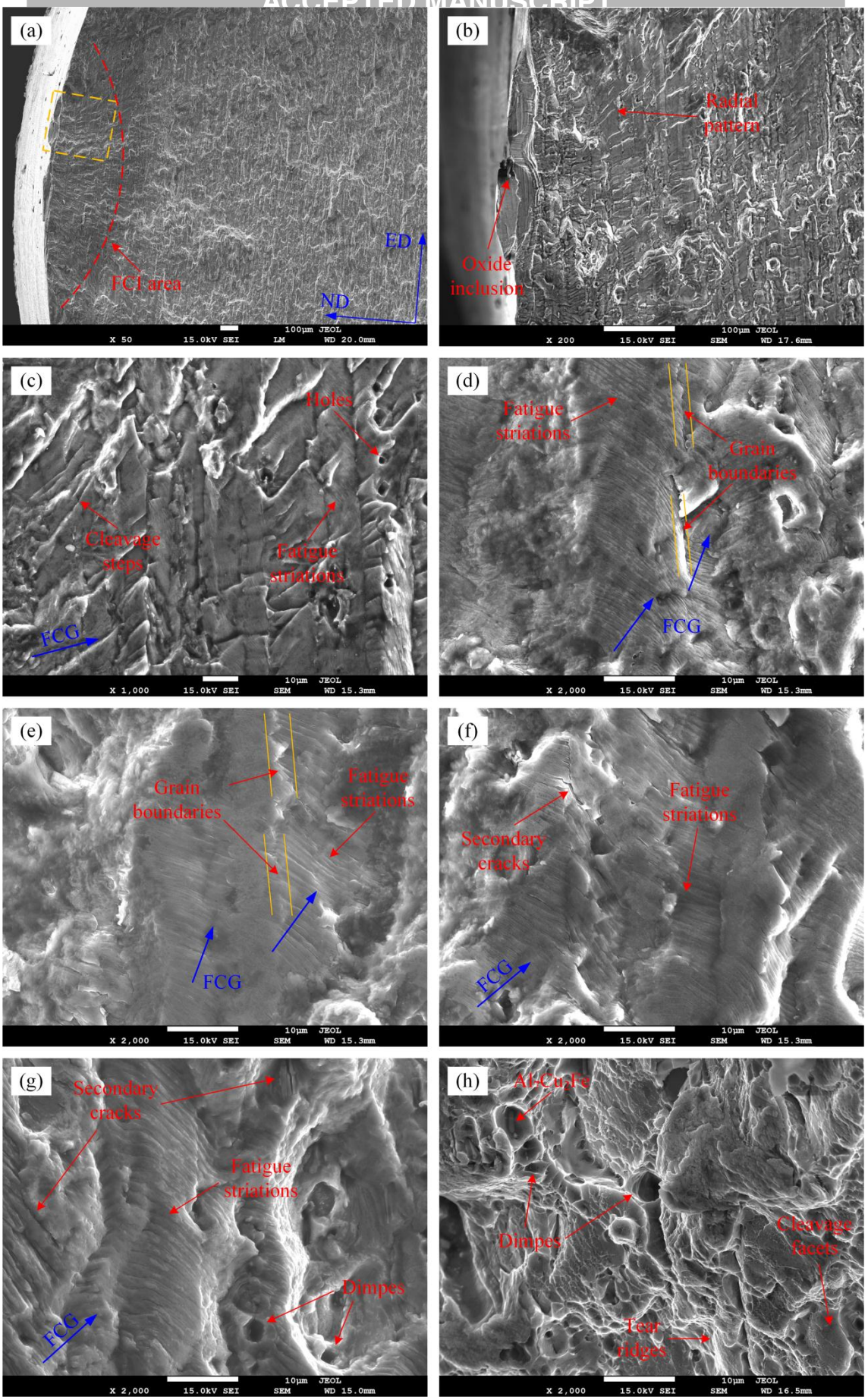

Fig. 13. SEM images of fatigue fracture surface of TD samples at the strain amplitude of 0.5%: (a–b) FCI zone, (c)

transition zone from early crack growth to stable crack growth, (d–g) FCG zone, and (h) final fracture zone.

Fig. 14 gives the fatigue fractography of ED samples at the strain amplitude of 0.5%. The typical fatigue fractography consisting of three zones can also be observed. The FCI zone in Fig. 14(a) presents a slightly radial pattern, and the crack originates at the sample surface. It is similar to TD samples that a few oxide inclusions are observed in this region. The morphology in the rectangle region in Fig. 14(a) is magnified as Fig. 14(b) which shows a transition zone from early to stable crack growth. This region presents a characteristic of cleavage steps as well, and a few fatigue striations with quite small spacing are found locally. The FCG zone in Fig. 14(c) and (d) shows the existence of fatigue striations, but the striations in this zone are distributed less extensively than those of TD samples in Fig. 13. The striations in different grains have slightly different propagation directions, and some tire-like striations appears on certain planes in Fig. 14(c). In the late stage of FCG, the spacing of fatigue striations increases apparently and the shape of striations becomes irregular, as shown in Fig. 14(d). It is different from TD samples that the grain morphology of ED fracture surface is unobvious in the FCG zone. The final fracture zone in Fig. 14(e) is dominated by many of cleavage facets of different area, and there are many fine dimples and some tear ridges among facets. The ductile fracture in this region is unobvious, which is different from TD final fracture zone. In conclusion, at low strain amplitude of 0.5%, the fatigue features in FCI and FCG zones of TD samples have certain similarity with those of ED ones, while the final fracture zones are clearly different.

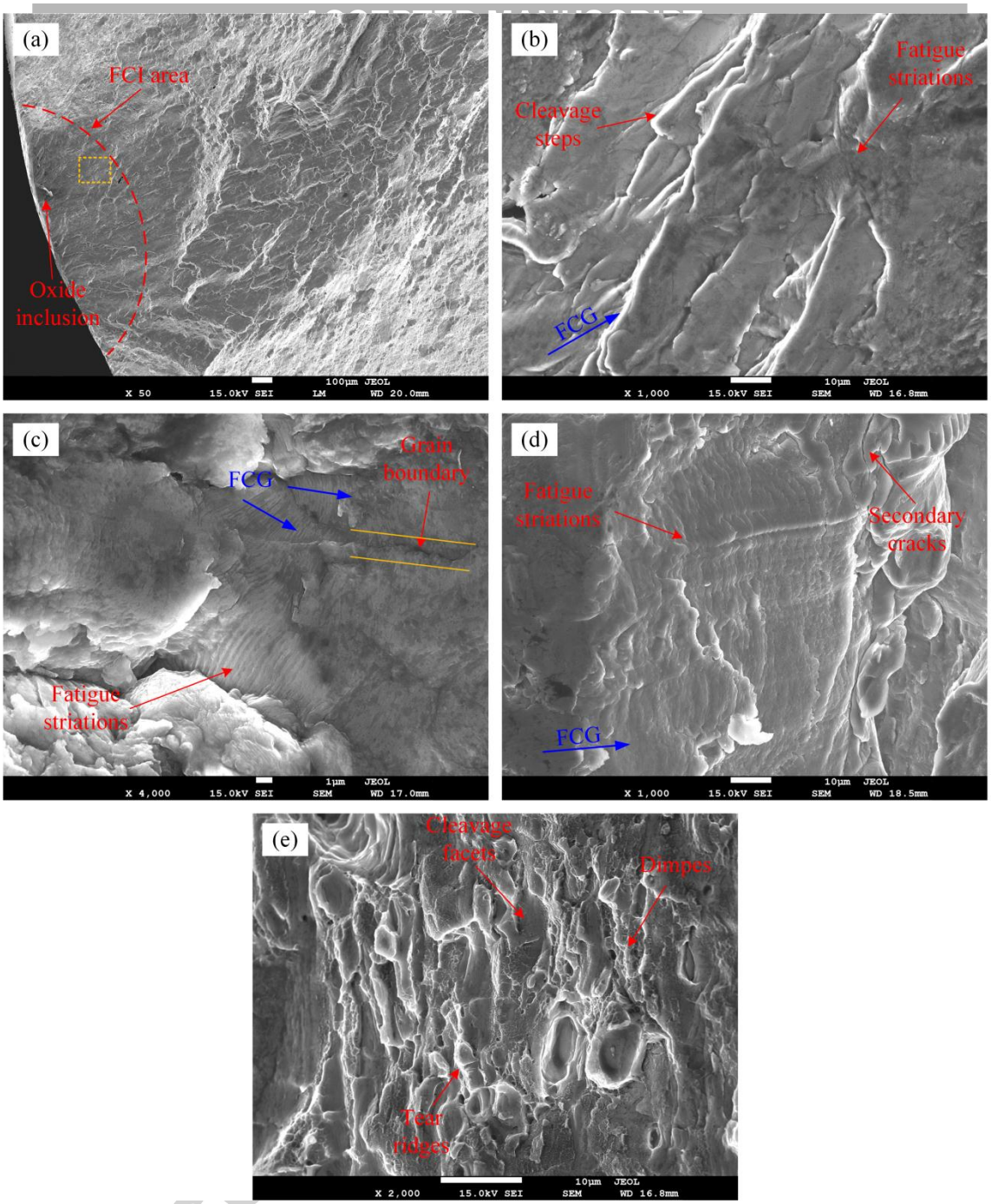

Fig. 14. SEM images of fatigue fracture surface of ED samples at the strain amplitude of 0.5%: (a) FCI zone, (b) transition zone from early crack growth to stable crack growth, (c–d) FCG zone, and (e) final fracture zone.

5. 2. Fatigue fractography at high strain amplitude

Fig. 15 gives the fatigue fractography of TD samples at the strain amplitude of 1.0%. Multiple FCI areas are located on the surface of the samples in Fig. 15(a), and the radial pattern disappears. During cyclic loading at higher strain amplitude, the cracks tend to occur at more than one locations meanwhile, and the FCI zone occupies a smaller area of the fracture surface. Fig. 15(b), (c) and (d) present magnified morphologies of the rectangle region Ⅰ, Ⅱ and Ⅲ in Fig. 15(a), respectively. The morphology of early crack growth stage is shown as Fig. 15(b), which is characterized by lots of cleavage planes along with a few small dimples distributed on grain boundaries.

It is of interest that there are many circular shallow pits with different sizes on the cleavage planes. These pits probably derive from the micro holes which form on the interfaces between the matrix and second phase particles under early cycle loading. In the late crack growth stage in Fig. 15(c), the number and size of dimples increase while the number of circular pits decreases, and the cleavage characteristic is relieved. Note that fatigue striations completely disappear in this FCG zone due to shorter fatigue life at high strain amplitude, but the grain morphology can be observed as similar to the FCG zone in Fig. 13. In the final fracture zone in Fig. 15(d), many dimples of larger size and depth can be found and these dimples may connect with each other during their nucleation and growth. This zone which presents an obvious ductile fracture characteristic, which is similar to quasi-static tensile fracture surface. In addition, partial tear ridges and fewer circular pits are also observed.

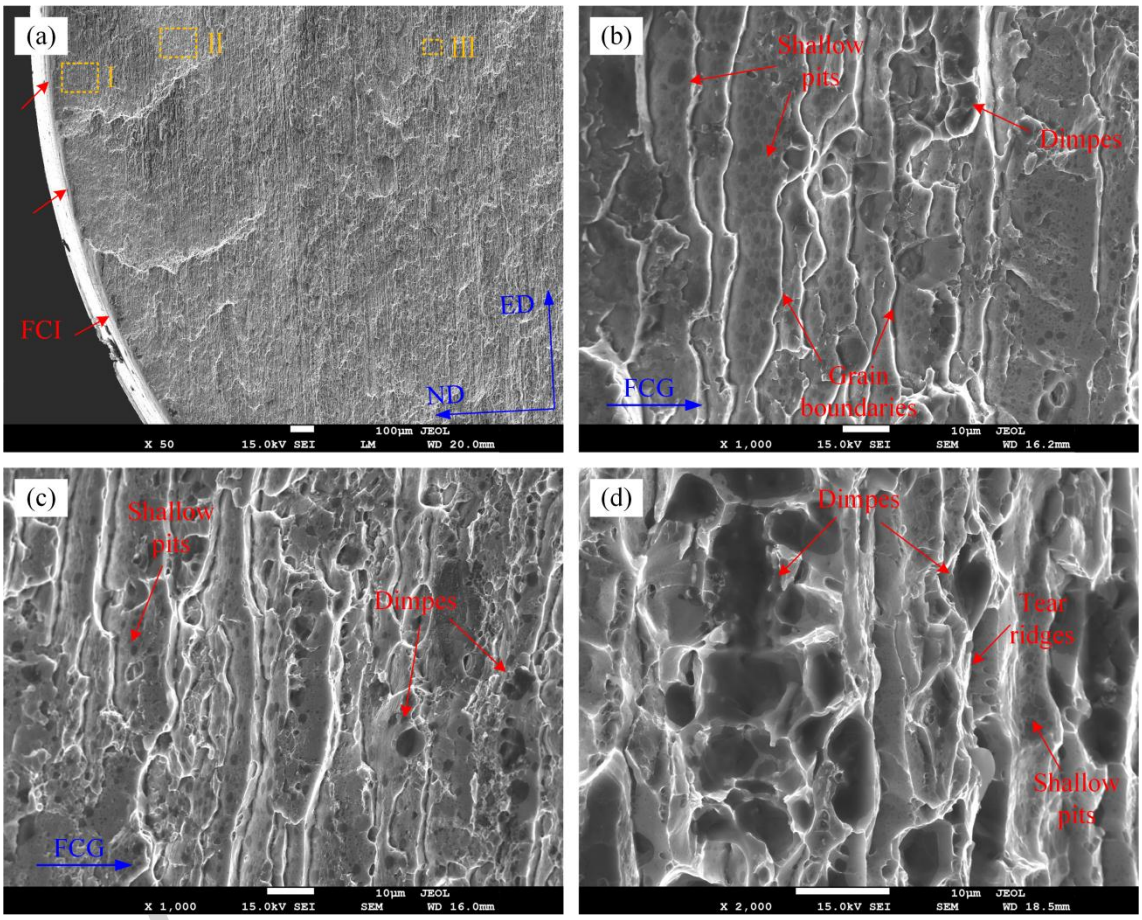

Fig. 15. SEM images of fatigue fracture surface of TD samples at the strain amplitude of 1.0%: (a) FCI zone, (b–c) FCG zone, and (d) final fracture zone.

Fig. 16 gives the fatigue fractography of ED samples at the strain amplitude of 1.0%. There are also multiple traces of crack initiation on the surface of the samples in Fig. 16(a). Fig. 16(b), (c) and (d) present magnified morphologies of the region Ⅰ, Ⅱ and Ⅲ in Fig. 16(a), respectively. The morphologies of both early and late crack growth stage are similar to those of TD samples in Fig. 15, e.g., the fatigue striations is also absent and the grain morphology can also be observed. However, there are a few differences that circular shallow pits basically

disappear, and the traces of crack between grains in the late stage are more obvious, as shown in Fig. 16(c). The final fracture zone in Fig. 16(d) is more similar to that at 0.5% in Fig. 14(e), but the dimples of irregular shape have a larger size and depth suggesting a more obvious ductile fracture characteristic. However, the ductile characteristic of the final fracture zone of ED samples is much weaker than TD samples at both 0.5% and 1.0% strain amplitude in general.

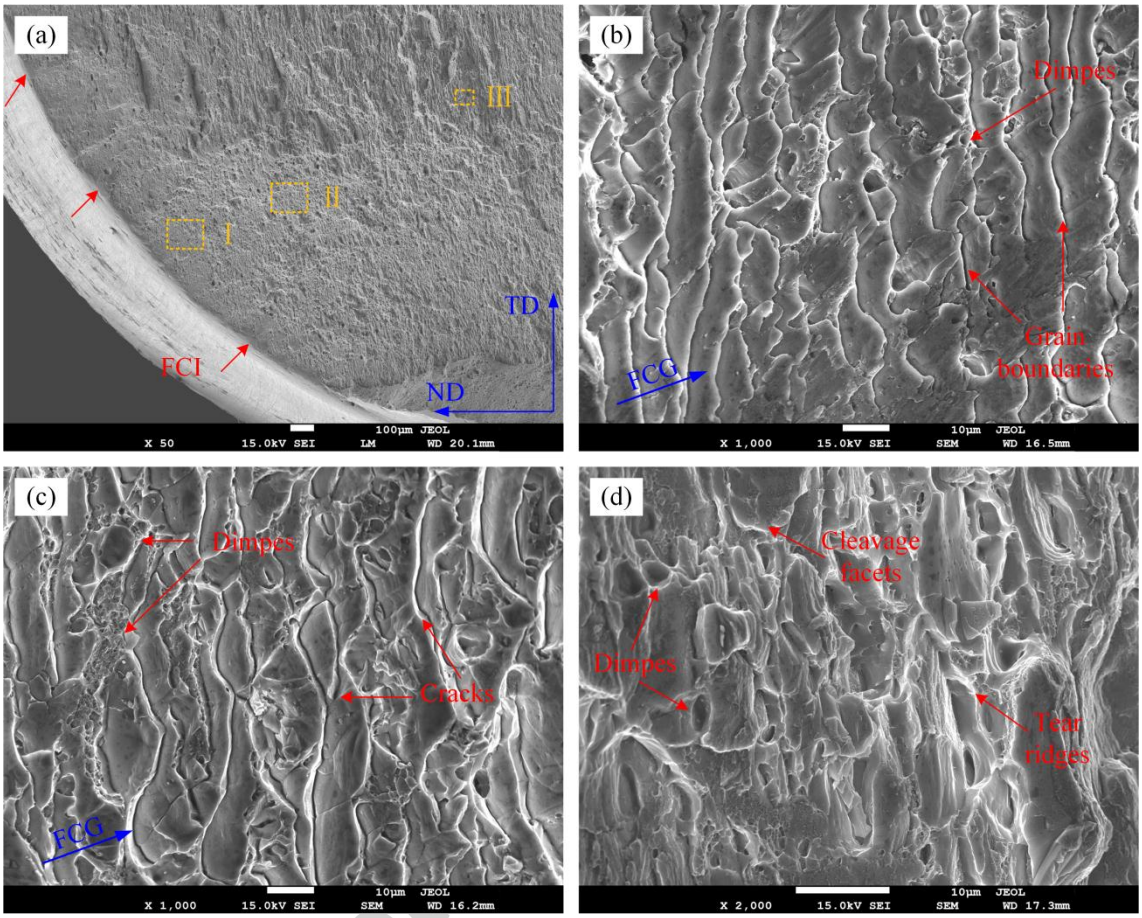

Fig. 16. SEM images of fatigue fracture surface of ED samples at the strain amplitude of 1.0%: (a) FCI zone, (b–c) FCG zone, and (d) final fracture zone.

5. 3. deformation microstructure

Fig. 17 gives the deformation microstructure near fatigue fracture surfaces of ED samples at the strain amplitude of 0.5% and 1.0%. Fig. 17(b) and (d) are magnified images for the rectangle region of Fig. 17(a) and (c), respectively. After cycle loading, the deformed grains are distributed extensively in the alloy, and there are lots of dislocation structures within these grains. Compared with the microstructure at 0.5% strain amplitude, the number of deformed grains in the alloy and the density of dislocations within grains are high at 1.0%. The dislocations are continuously generated and driven within grains under the action of cycle stress, and pile up in front of the (sub)grain boundaries (shown in Fig. 17(a), (c)) and secondary phase particles (shown in Fig. 17(b), (d)) due to the inhibition of these structures, leading to an high-density aggregation state of dislocations. In addition, some

evolved dislocation structures (dislocation loops, dislocation tangles, etc.), interact with subsequent dislocations, and also play a strong pinning effect against the movement of dislocations [49, 60], where dislocation loops form around hard-to-shear precipitates during the dislocation slip and dislocation tangles are caused by the movement of multiple slip systems. Therefore, under the loading condition of constant strain amplitude, the dislocation slip requires higher stress to drive against the pinning effect, thereby presenting a cyclic hardening behavior as shown in Fig. 9. Meanwhile, the density of dislocations in front of the obstructions increases gradually with the number of cycles, and early micro-cracks tend to form in these stress concentration areas.

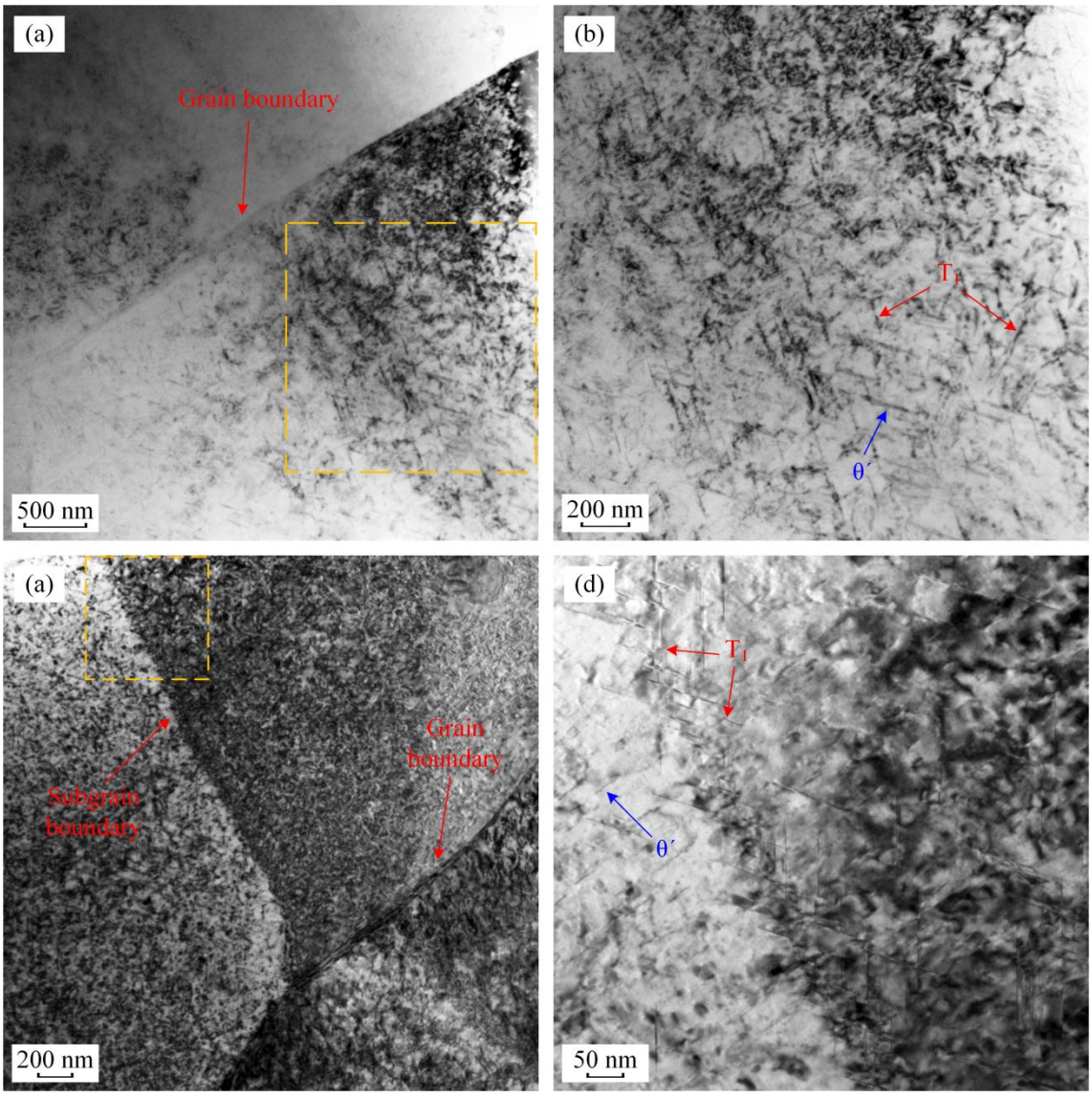

Fig. 17. TEM images of the deformation microstructure near fatigue fracture surfaces of ED samples at the strain amplitude of (a), (b) 0.5% and (c), (d) 1.0%.

At the strain amplitude of 0.5%, the early cyclic hardening stage is followed by cyclic stability in Fig. 9, which may be caused by the following factors: (1) The dislocation structures which have formed in the cycle hardening stage react on dislocation sources and decrease the multiplication of dislocations, leading to the

improvement of the yield threshold. Then, the material produces less and less plastic deformation gradually at constant strain amplitude, and thus both the microstructure and cycle stress amplitude can keep in a stable state at the late stage. (2) The dislocation pile-ups and tangles can promote the activation of cross slip and the formation of secondary slip planes during the cyclic deformation process. Besides, Aluminum is on kind of face-centered cubic metal with high stacking fault energy, and the cross slip is likely to be generated within deformed alloys. Then, the cross slip could also enhance the annihilation of opposite sign dislocations further [61, 62]. Therefore, the dislocation density does not continue to increase, and the cycle hardening effect is neutralized, resulting in that the cycle stress remains almost constant after reaching a maximum level. (3) In the later stage of fatigue loading, the cracks have originated at the sample surface and gradually propagate toward the inside of the material, which may cause that the cycle stress cannot increase continuously. In contrast, under the high load condition of 1.0% strain amplitude, the cyclic stress increases continuously and rapidly as shown in Fig. 9, indicating that the density of dislocations keeps increasing and the cycle hardening effect always plays a dominant role within the limited fatigue life.

Note that coherent ordered precipitates δ′ in the binary Al–Li alloys are generally susceptible to the dislocation shearing, which leads to the formation of planar slip bands during the cyclic deformation process. The planar slip bands can further cause heterogeneous deformation microstructure and eliminate the cyclic hardening effect. However, in the aged AA2195 with a high Cu/Li ratio under the heat treatment condition in this work, the δ′ phase is nearly absent, and the planar slip bands are not observed in the deformation microstructure after LCF tests. Moreover, numbers of precipitates T_1 extensively distributed in the aged AA2195 also effectively hinder the formation of plane slip band, and weaken the tendency strain localization. Therefore, the cycle softening effect due to planar slip bands is probably absent, which partly indicates that homogeneous plastic deformation and microstructure are generated in the alloy under cycle loading.

Conclusion

The microstructure analysis and strain-controlled low-cycle fatigue tests for spray-formed AA2195 extruded plate after aging treatment were performed. The fatigue fracture mode and dislocation microstructure after cycle deformation under different loading conditions were also investigated. The following conclusions could be drawn in this work:

(1) The extruded plate, which was dominated by elongated unrecrystallized grains, had a rolling-type texture along extrusion direction with the highest intensity at Brass component. There were numbers of large-sized secondary phase particles, such as Al_7Cu_2Fe and Al_2Cu, on grain boundaries. The existence of fine precipitates T_1

played a vital role in the strengthening of aged AA2195, while δ′ phase was basically absent.

(2) At the cycle loading condition of 0.4% strain amplitude, the alloy was basically in elastic deformation state, which presented a cycle stability behavior. At 0.5% strain amplitude, the initial cyclic hardening was followed by a cyclic stability. At higher strain amplitudes (0.6–1.0%), only a continuously and rapidly increasing cycle hardening behavior could be found until fatigue fracture. Moreover, the alloy always had a higher cycle stress amplitude along ED than TD at each strain amplitude.

(3) Both TD and ED samples showed a similar fatigue life at the same strain condition. The fatigue life models based on the plastic strain energy and the total strain energy were built, respectively, and the latter gave a more accurate prediction for AA2195 in both two sample directions.

(4) At 0.5% strain amplitude, the fatigue fracture surfaces consisted of FCI zone, FCG zone and final fracture zone, and the FCG zone had a typical characteristic of fatigue striations. At 1.0% strain amplitude, multiple cracks originated on the sample surface, fatigue striations completely disappeared, and the final fracture zone contained numerous dimples. In contrast with ED samples, the fatigue fractography of TD samples had a strong ductile fracture characteristic.

(5) Compared with the deformation microstructure at 0.5% strain amplitude, the deformation extent and the dislocation density within the alloy were generally high at 1.0%. The cyclic hardening was closely associated with the interaction between moving dislocations and obstacles against them, while the cycle stability was dependent on the microstructure stabilization. Moreover, the cycle softening effect resulting from the δ′ phase sheared by dislocation movement was basically absent.

Acknowledgments

The authors would like to acknowledge financial support from National Natural Science Foundation of China (51575315, 51735008) Science Fund for Distinguished Young Scholars of Shandong Province (JQ201810) and the Key Research and Development Program of Shandong Province (2017GGX30140).

References

[1] X. Zhang, Y. Chen, J. Hu, Recent advances in the development of aerospace materials, Prog. Aerosp. Sci. 97 (2018) 22–34.

[2] T. Dursun, C. Soutis, Recent developments in advanced aircraft aluminium alloys, Mater. Des. 56 (2014) 862–871.

[3] A. Abd El-Aty, Y. Xu, X. Guo, S.H. Zhang, Y. Ma, D. Chen, Strengthening mechanisms, deformation behavior,

and anisotropic mechanical properties of Al-Li alloys: A review, J. Adv. Res. 10 (2018) 49–67.

[4] R.J. Rioja, J. Liu, The evolution of Al-Li base products for aerospace and space applications, Metall. Mater. Trans. A 43 (9) (2012) 3325–3337.

[5] R. Yoshimura, T.J. Konno, E. Abe, K. Hiraga, Transmission electron microscopy study of the evolution of precipitates in aged Al–Li–Cu alloys: The θ′ and T_1 phases, Acta Mater. 51 (14) (2003) 4251–4266.

[6] K.S. Kumar, S.A. Brown, J.R. Pickens, Microstructural evolution during aging of an AlCuLiAgMgZr alloy, Acta Mater. 44 (5) (1996) 1899–1915.

[7] B.I. Rodgers, P.B. Prangnell, Quantification of the influence of increased pre-stretching on microstructure-strength relationships in the Al–Cu–Li alloy AA2195, Acta Mater. 108 (2016) 55–67.

[8] T. Dorin, A. Deschamps, F.D. Geuser, C. Sigli, Quantification and modelling of the microstructure/strength relationship by tailoring the morphological parameters of the T_1 phase in an Al–Cu–Li alloy, Acta Mater. 75 (2014) 134–146.

[9] B.M. Gable, A.W. Zhu, A.A. Csontos, E.A. Starke Jr., The role of plastic deformation on the competitive microstructural evolution and mechanical properties of a novel Al–Li–Cu–X alloy, J. Light Met. 1 (1) (2001) 1–14.

[10] W.A. Cassada, G.J. Shiflet, E.A. Starke, The effect of plastic deformation on Al_2CuLi (T_1) precipitation, Metall. Trans. A 22 (2) (1991) 299–306.

[11] P.S. De, R.S. Mishra, J.A. Baumann, Characterization of high cycle fatigue behavior of a new generation aluminum lithium alloy, Acta Mater. 59 (15) (2011) 5946–5960.

[12] M.C. Chaturvedi, D.L. Chen, Effect of specimen orientation and welding on the fracture and fatigue properties of 2195 Al–Li alloy, Mater. Sci. Eng. A. 387–389 (2004) 465–469.

[13] N.D. Alexopoulos, E. Migklis, A. Stylianos, D.P. Myriounis, Fatigue behavior of the aeronautical Al–Li (2198) aluminum alloy under constant amplitude loading, Int. J. Fatigue 56 (2013) 95–105.

[14] L. Xu, Q. Wang, M. Zhou, Micro-crack initiation and propagation in a high strength aluminum alloy during very high cycle fatigue, Mater. Sci. Eng. A 715 (2018) 404–413.

[15] M.R. Joyce, M.J. Starink, I. Sinclair, Assessment of mixed mode loading on macroscopic fatigue crack paths in thick section Al–Cu–Li alloy plate, Mater. Des. 93 (2016) 379–387.

[16] D.F. Metz, M.E. Barkey, Fatigue behavior of friction plug welds in 2195 Al–Li alloy, Int. J. Fatigue 43 (2012) 178–187.

[17] P.M.G.P. Moreira, A.M.P. de Jesus, M.A.V. de Figueiredo, M. Windisch, G. Sinnema, P.M.S.T. de Castro, Fatigue and fracture behaviour of friction stir welded aluminium–lithium 2195, Theor. Appl. Fract. Mech. 60

(1) (2012) 1–9.

[18] O. Hatamleh, M. Hill, S. Forth, D. Garcia, Fatigue crack growth performance of peened friction stir welded 2195 aluminum alloy joints at elevated and cryogenic temperatures, Mater. Sci. Eng. A 519 (1–2) (2009) 61–69.

[19] N. Eswara Prasad, P. Rama Rao, Low cycle fatigue resistance of Al–Li alloys, Mater. Sci. Technol. 16 (4) (2000) 408–426.

[20] M. Lewandowska, J. Mizera, J.W. Wyrzykowski, Cyclic behaviour of model Al–Li alloys: Effect of the precipitate state, Mater. Charact. 45 (3) (2000) 195–202.

[21] K.T.V. Rao, R.O. Ritchie, Fatigue of aluminium–lithium alloys, Int. Mater. Rev. 37 (1) (1992) 153–186.

[22] A.A. Csontos, E.A. Starke, The effect of inhomogeneous plastic deformation on the ductility and fracture behavior of age hardenable aluminum alloys, Int. J. Plast. 21 (6) (2005) 1097–1118.

[23] A. Deschamps, B. Decreus, F. De Geuser, T. Dorin, M. Weyland, The influence of precipitation on plastic deformation of Al–Cu–Li alloys, Acta Mater. 61 (11) (2013) 4010–4021.

[24] T. Dorin, F. De Geuser, W. Lefebvre, C. Sigli, A. Deschamps, Strengthening mechanisms of T_1 precipitates and their influence on the plasticity of an Al–Cu–Li alloy, Mater. Sci. Eng. A 605 (2014) 119–126.

[25] D. Khireddine, R. Rahouadj, M. Clavel, The influence of δ′ and s′ precipitation on low cycle fatigue behaviour of an aluminium alloy, Acta Metall. 37 (1) (1989) 191–201.

[26] S.M. Liu, Z.G. Wang, Fatigue properties of 8090 Al–Li alloy processed by equal-channel angular pressing, Scr. Mater. 48 (10) (2003) 1421–1426.

[27] M. Wang, Z. Liu, Z. Liu, S. Yang, Y. Weng, T. Song, Effects of Sc on microstructure and low-cycle fatigue properties of Al–Li alloy, Mater. Sci. Eng. A 483–484 (2008) 448–451.

[28] W.Z. Han, A. Vinogradov, C.R. Hutchinson, On the reversibility of dislocation slip during cyclic deformation of Al alloys containing shear-resistant particles, Acta Mater. 59 (9) (2011) 3720–3736.

[29] K. Hockauf, M.F.X. Wagner, T. Halle, T. Niendorf, M. Hockauf, T. Lampke, Influence of precipitates on low-cycle fatigue and crack growth behavior in an ultrafine-grained aluminum alloy, Acta Mater. 80 (2014) 250–263.

[30] N. Nayan, S.V.S. Narayana Murty, A.K. Jha, B. Pant, S.C. Sharma, K.M. George, G.V.S. Sastry, Mechanical properties of aluminium–copper–lithium alloy AA2195 at cryogenic temperatures, Mater. Des. 58 (2014) 445–450.

[31] N. Nayan, S.V.S. Narayana Murty, A.K. Mukhopadhyay, K.S. Prasad, A.K. Jha, B. Pant, S.C. Sharma, K.M. George, Ambient and cryogenic tensile properties of AA2195T87 sheets with pre-aging cold work by a

combination of cold rolling and stretching, Mater. Sci. Eng. A 585 (2013) 475–479.

[32] M. Suresh, A. Sharma, A.M. More, N. Nayan, S. Suwas, Effect of Scandium addition on evolution of microstructure, texture and mechanical properties of thermo-mechanically processed Al-Li alloy AA2195, J. Alloys Compd. 740 (2018) 364–374.

[33] J. Tao, L. Zhang, G. Wu, A. Chen, X. Zhang, C. Shi, Effect of heat treatment on the microstructure and mechanical properties of extruded Al–4Cu–1Li–0.4Mg–0.4Ag–0.18Zr Alloy, Mater. Sci. Eng. A 717 (2018) 11–19.

[34] J.H. Kim, J.H. Jeun, H.J. Chun, Y.R. Lee, J.T. Yoo, J.H. Yoon, H.S. Lee, Effect of precipitates on mechanical properties of AA2195, J. Alloys Compd. 669 (2016) 187–198.

[35] H. Qin, H. Zhang, H. Wu, The evolution of precipitation and microstructure in friction stir welded 2195-T8 Al–Li alloy, Mater. Sci. Eng. A 626 (2015) 322–329.

[36] N. Nayan, S.V.S.N. Murty, A.K. Jha, B. Pant, S.C. Sharma, K.M. George, G.V.S. Sastry, Processing and characterization of Al–Cu–Li alloy AA2195 undergoing scale up production through the vacuum induction melting technique, Mater. Sci. Eng. A 576 (2013) 21–28.

[37] N. Nayan, S.V.S.N. Murty, S. Chhangani, A. Prakash, M.J.N.V. Prasad, I. Samajdar, Effect of temperature and strain rate on hot deformation behavior and microstructure of Al-Cu-Li alloy, J. Alloys Compd. 723 (2017) 548–558.

[38] Q. Yang, X. Wang, X. Li, Z. Deng, Z. Jia, Z. Zhang, G. Huang, Q. Liu, Hot deformation behavior and microstructure of AA2195 alloy under plane strain compression, Mater. Charact. 131 (2017) 500–507.

[39] Y. Yang, F. Ma, H.B. Hu, Q.M. Zhang, X.W. Zhang, Microstructure evolution of 2195 Al–Li alloy subjected to high-strain-rate deformation, Mater. Sci. Eng. A 606 (2014) 299–303.

[40] N. Jiang, X. Gao, Z.Q. Zheng, Microstructure evolution of aluminum-lithium alloy 2195 undergoing commercial production, Trans. Nonferrous Met. Soc. China 20 (5) (2010) 740–745.

[41] E. Balducci, L. Ceschini, S. Messieri, S. Wenner, R. Holmestad, Effects of overaging on microstructure and tensile properties of the 2055 Al-Cu-Li-Ag alloy, Mater. Sci. Eng. A 707 (2017) 221–231.

[42] F.A. Tchitembo Goma, D. Larouche, A. Bois-Brochu, C. Blais, J. Boselli, M. Brochu, Effect of extrusion aspect ratio and test temperatures on fatigue crack growth behavior of a 2099-T83 Al–Li alloy, Int. J. Fatigue 59 (2014) 244–253.

[43] A. Bois-Brochu, C. Blais, F.A.T. Goma, D. Larouche, J. Boselli, M. Brochu, Characterization of Al–Li 2099 extrusions and the influence of fiber texture on the anisotropy of static mechanical properties, Mater. Sci. Eng. A 597 (2014) 62–69.

[44] S.J. Hales, R.A. Hafley, Texture and anisotropy in Al-Li alloy 2195 plate and near-net-shape extrusions, Mater. Sci. Eng. A 257 (1) (1998) 153–164.

[45] H. Li, Y. Tang, Z. Zeng, Z. Zheng, F. Zheng, Effect of ageing time on strength and microstructures of an Al-Cu-Li-Zn-Mg-Mn-Zr alloy, Mater. Sci. Eng. A 498 (1–2) (2008) 314–320.

[46] H. Li, D. Huang, W. Kang, J. Liu, Y. Ou, D. Li, Effect of Different Aging Processes on the Microstructure and Mechanical Properties of a Novel Al–Cu–Li Alloy, J. Mater. Sci. Technol. 32 (10) (2016) 1049–1053.

[47] Z.R. Pan, Z.Q. Zheng, Z.Q. Liao, S.C. Li, New cubic precipitate in Al–3.5Cu–1.0Li–0.5In (wt.%) alloy, Mater. Lett. 64 (8) (2010) 942–944.

[48] B. Decreus, A. Deschamps, F. De Geuser, P. Donnadieu, C. Sigli, M. Weyland, The influence of Cu/Li ratio on precipitation in Al–Cu–Li–x alloys, Acta Mater. 61 (6) (2013) 2207–2218.

[49] K.L. Fan, X.S. Liu, G.Q. He, H. Chen, Elevated temperature low cycle fatigue of a gravity casting Al–Si–Cu alloy used for engine cylinder heads, Mater. Sci. Eng. A 632 (2015) 127–136.

[50] C. Shi, X.G. Chen, Effect of Zr addition on hot deformation behavior and microstructural evolution of AA7150 aluminum alloy, Mater. Sci. Eng. A 596 (2014) 183–193.

[51] A.A. Gokhale, V. Singh, Effect of Zr content and mechanical working on the structure and tensile properties of AA8090 alloy plates, J. Mater. Process. Technol. 159 (3) (2005) 369–376.

[52] S.K. Shaha, F. Czerwinski, W. Kasprzak, J. Friedman, D.L. Chen, Effect of Mn and heat treatment on improvements in static strength and low-cycle fatigue life of an Al–Si–Cu–Mg alloy, Mater. Sci. Eng. A 657 (2016) 441–452.

[53] R. Liu, Z.J. Zhang, P. Zhang, Z.F. Zhang, Extremely-low-cycle fatigue behaviors of Cu and Cu–Al alloys: Damage mechanisms and life prediction, Acta Mater. 83 (2015) 341–356.

[54] M. Wang, J.C. Pang, S.X. Li, Z.F. Zhang, Low-cycle fatigue properties and life prediction of Al-Si piston alloy at elevated temperature, Mater. Sci. Eng. A 704 (2017) 480–492.

[55] K.N. Smith, P. Watson, T.H. Topper, A stress-strain function for the fatigue of metals, J. Mater. 5 (4) (1970) 767–778.

[56] Q. Zhang, Z. Zuo, J. Liu, High-temperature low-cycle fatigue behaviour of a cast Al–12Si–CuNiMg alloy, Fatigue Fract. Eng. Mater. Struct. 36 (7) (2013) 623–630.

[57] M.S. Song, Y.Y. Kong, M.W. Ran, Y.C. She, Cyclic stress-strain behavior and low cycle fatigue life of cast A356 alloys, Int. J. Fatigue 33 (12) (2011) 1600–1607.

[58] K. Golos, F. Ellyin, A total strain energy density theory for cumulative fatigue damage, ASME J. Pressure Vessel Technol. 110 (1) (1988) 36–41.

[59] J.A. Abdalla, R.A. Hawileh, F. Oudah, K. Abdelrahman, Energy-based prediction of low-cycle fatigue life of BS 460B and BS B500B steel bars, Mater. Des. 30 (10) (2009) 4405–4413.

[60] J. Liu, Q. Zhang, Z. Zuo, Y. Xiong, F. Ren, A.A. Volinsky, Microstructure evolution of Al–12Si–CuNiMg alloy under high temperature low cycle fatigue, Mater. Sci. Eng. A 574 (2013) 186–190.

[61] W. Püschl, Models for dislocation cross-slip in close-packed crystal structures: A critical review, Prog. Mater. Sci. 47 (4) (2002) 415–461.

[62] M.S. Pham, C. Solenthaler, K.G.F. Janssens, S.R. Holdsworth, Dislocation structure evolution and its effects on cyclic deformation response of AISI 316L stainless steel, Mater. Sci. Eng. A 528 (7–8) (2011) 3261–3269.